

**The role of magnetic boundaries in kinematic and self-consistent magnetohydrodynamic simulations of precession-driven dynamo action in a closed cylinder.**

André Giesecke,<sup>1</sup> Mike Wilbert,<sup>2</sup> Ján Šimkanin,<sup>1,3</sup> Rainer Grauer,<sup>2</sup> and Frank Stefani<sup>1</sup>

<sup>1</sup>*Institute of Fluid Dynamics, Helmholtz-Zentrum Dresden-Rossendorf, Bautzner Landstrasse 400, D-01328 Dresden, Germany*

<sup>2</sup>*Institut für theoretische Physik I, Ruhr Universität Bochum, D-44780 Bochum, Germany*

<sup>3</sup>*Institute of Geophysics, Czech Academy of Sciences, Boční II/1401, 141 00 Prague 4 – Spořilov, Czech Republic*

(\*Electronic mail: [a.giesecke@hzdr.de](mailto:a.giesecke@hzdr.de))

(Dated: 7 April 2025)

We numerically examine dynamo action generated by a flow of an electrically conducting fluid in a precessing cylindrical cavity. We compare a simplified kinematic approach based on the solution of the magnetic induction equation with a prescribed velocity field with the results from a self-consistent three-dimensional simulation of the complete set of magnetohydrodynamic equations.

In all cases, we observe a minimum for the onset of dynamo action in a transitional regime, within which the hydrodynamic flow undergoes a change from a large-scale to a more small-scale, turbulent behaviour. However, significant differences in the absolute values for the critical magnetic Reynolds number occur depending on the physical properties of the external layers surrounding the flow active domain. The strong influence of the electromagnetic properties of outer layers with the large variation of the critical magnetic Reynolds number can be related to the existence of two different branches with dynamo action.

In contrast to the kinematic models, the nonlinear MHD simulations reveal a small scale dynamo solution with the magnetic energy remaining significantly smaller than the kinetic energy of the flow. In irregular intervals, we observe dynamo bursts with a local concentration of the magnetic field, resulting in a global increase of the magnetic energy by a factor of 3 to 5. However, diffusion of the local patches caused by strong local shear is too rapid, causing these features to exist for only a short period so that their dynamical impact on the dynamo remains small. As the magnetic field is small-scale and weak, the nonlinear feedback on the flow through the Lorentz force remains small and arises essentially in terms of a slight damping of the fast timescales, whereas there is no noticeable change in flow amplitude compared to the hydrodynamic case.

A connection with the kinematic models can be derived by looking at the time-averaged field of the MHD dynamo solution. This is comparable to the eigenmode of the inefficient branch of the kinematic models, which explains their large critical magnetic Reynolds number.

## I. INTRODUCTION

The experimental investigation of magnetic field generation through a flow of electrically conductive fluid is of great interest, as such a magnetohydrodynamic dynamo process is crucial for many astrophysical bodies and allows conclusions about their evolution and internal structure. Following the successful first-generation dynamo experiments in Karlsruhe<sup>1</sup> and Riga<sup>2</sup>, which confirmed the fundamental principle, subsequent dynamo experiments in Cadarache (Monchaux *et al.*<sup>3</sup>) revealed a wide variety of different dynamic behaviours. Currently, a new experiment is being set up at HZDR (Stefani *et al.*<sup>4</sup>). In the DRESHDYN experiment, a flow of liquid sodium in a precessing cylinder is intended to generate a magnetic field. Precession is a repeatedly proposed driving mechanism for natural dynamos, whether for the Moon<sup>5</sup> or for the Earth<sup>6</sup>. Regarding the Lunar dynamo, which around 4 billion years ago generated a magnetic field of comparable strength to that of today's Earth, precession is indeed the most promising candidate to explain the observations including the disappearance of the dynamo about 3 billion years ago (see e.g. Stys and Dumberry<sup>7</sup>). One of the main reasons to consider precession driven dynamo action for the geodynamo are paleomagnetic records, which suggest that the geodynamo was active even before the formation of the Earth's solid inner core. This, in turn, implies that thermochemical convection, driven by the cooling and crystallization of the core, was not always the primary mechanism and before the onset of thermochemical convection, alternative mechanisms must have driven the early geodynamo. Support for this hypothesis comes from recent experiments and numerical computations that yield rather large values for the heat conductivity under conditions typical for the Earth's liquid core, which imposes strict energetic constraints for the convective state, particularly for the early geodynamo before the formation of the solid inner Earth's core (see e.g. Olson<sup>8</sup>, Landeau *et al.*<sup>9</sup>). While it is relatively clear that the laminar flow directly driven by precession is energetically insignificant (Rochester *et al.*<sup>10</sup>), the original idea of Malkus was based on a turbulent base state<sup>6</sup>, which was later underpinned by estimates of an upper limit to (viscous) dissipation by Kerswell<sup>11</sup>. Indeed, precession-driven fluid flows exhibit several instabilities, allowing both forward and backward cascades of energy transfer (Pizzi *et al.*<sup>12</sup>) that end up in a flow state with small-scale turbulence superimposed by large-scale flow contributions essentially in terms of a circulation opposite to the original rotation of the container (Wilbert, Giesecke, and Grauer<sup>13</sup>, Giesecke

*et al.*<sup>14</sup>). This behaviour has also been observed in the laboratory<sup>15</sup> and so far various experiments have shown that precession is capable of generating strong flows, principally allowing for the large flow amplitudes required for the occurrence of the dynamo effect<sup>16–24</sup>. This contrasts with potentially more straightforward mechanisms, such as convection, which at typical laboratory scales may not achieve sufficiently vigorous flows due to lower driving efficiency<sup>25–27</sup>. Precession-driven dynamos also have been the subject of numerous numerical studies, and there are now successful dynamo simulations in all conceivable geometries, including spheres<sup>28</sup>, spheroids<sup>29</sup>, or cubes<sup>30</sup>. Nore *et al.*<sup>31</sup> and Cappanera *et al.*<sup>32</sup> investigated dynamo solutions in a cylindrical geometry comparable to the DRES-DYN experiment, but with small Reynolds numbers ( $\text{Re} \leq 4000$ ) and a rather large precession ratio of  $\text{Po} = 0.15$ . The induced magnetic fields showed a complex structure, which correspond most closely to a quadrupolar geometry. Preliminary investigations with particular regard to the DRES-DYN dynamo experiment utilized a kinematic model based on the geometry of the planned experiment and the large-scale flow from hydrodynamic simulations (Giesecke *et al.*<sup>33,34</sup>). These models showed that the dynamo effect works best in the narrow transition region that separates the subcritical from the supercritical state (Pizzi *et al.*<sup>35</sup>, Kumar *et al.*<sup>36</sup>). In the present study, we deepen the investigation of the dynamo effect in the transitional regime, investigate the influence of outer non-fluid layers, and compare kinematic models with a self-consistent magnetohydrodynamic (MHD) model to study the influence of the nonlinear terms and the Lorentz force feedback on the flow.

The present study is organized as follows. In section II, we introduce the equations that describe an electrically conducting fluid flow in a precessing cylinder and the related magnetic induction. We further summarize the essential response of the fluid to the forcing imposed by the precession of the container and present the evolution when the forcing is increased. The subsequent section III is dedicated to the results obtained from kinematic dynamo models, where only the induction equation is solved numerically assuming a prescribed, time-independent flow. In this section, we detail the impact of the electrical conductivity of the container. Section IV focuses on the corresponding results obtained from the full set of magnetohydrodynamic (MHD) equations and reveals differences and similarities with the kinematic dynamo. We end our study with the conclusions in section V, where we try to adopt our results for the forthcoming dynamo experiment at HZDR.



## II. SETUP OF THE KINEMATIC DYNAMO MODELS

### A. Equations and numerical methods

Initially, we focus on the kinematic problem, where only the magnetic induction equation is solved, and a time-independent velocity is prescribed, which is supposed to represent the mean (time-averaged) velocity in the experiment. Here we compare different configurations without and with outer layers of a conductive material surrounding the actual medium on which the force is exerted by the precession. The main finding from these models is a value for the critical magnetic Reynolds number, which is related to the minimum amplitude of the velocity field required for a dynamo to occur. The kinematic approach does neither consider the back-reaction of the magnetic field on the fluid flow via the Lorentz force nor the impact of small-scale fluctuations that could obstruct (turbulent diffusion) or support ( $\alpha$ -effect) the dynamo process.

We calculate the temporal evolution of the magnetic flux density  $\mathbf{B}$  (in the following called ‘magnetic field’) by numerically solving the magnetic induction equation, which reads

$$\frac{\partial \mathbf{B}}{\partial t} = \nabla \times \left( \mathbf{u} \times \mathbf{B} - \frac{1}{\text{Rm}} \nabla \times \mathbf{B} \right). \quad (1)$$

In Eq. (1)  $\mathbf{u}$  represents the (incompressible) velocity field and  $\text{Rm} = \Omega_c R^2 / \eta$  is the magnetic Reynolds number defined with the angular velocity  $\Omega_c$  of the cylinder, the radius  $R$  and the magnetic diffusivity  $\eta$  (see also Figure 1a). Assuming a prescribed time-independent flow field, Eq. (1) specifies a linear problem and the solution follows  $\mathbf{B}(\mathbf{r}, t) \propto e^{\kappa t}$  with the complex eigenvalue  $\kappa = \gamma + i\omega$  consisting of the growth rate (real part  $\gamma$ ) and the frequency (imaginary part  $\omega$ ). In order to solve Eq. (1) numerically, we use a finite volume approach in cylindrical coordinates. The scheme applies the constraint transport method to guarantee divergence-free solutions and is described in more detail in Giesecke, Stefani, and Gerbeth<sup>37</sup>. Extensive tests of the algorithm, in particular the impact of locally varying material properties, such as electrical conductivity and comparison with an alternative approach based on Spectral/Finite Elements (the SFEMaNS code<sup>38</sup>) can be found in Giesecke *et al.*<sup>39</sup>.

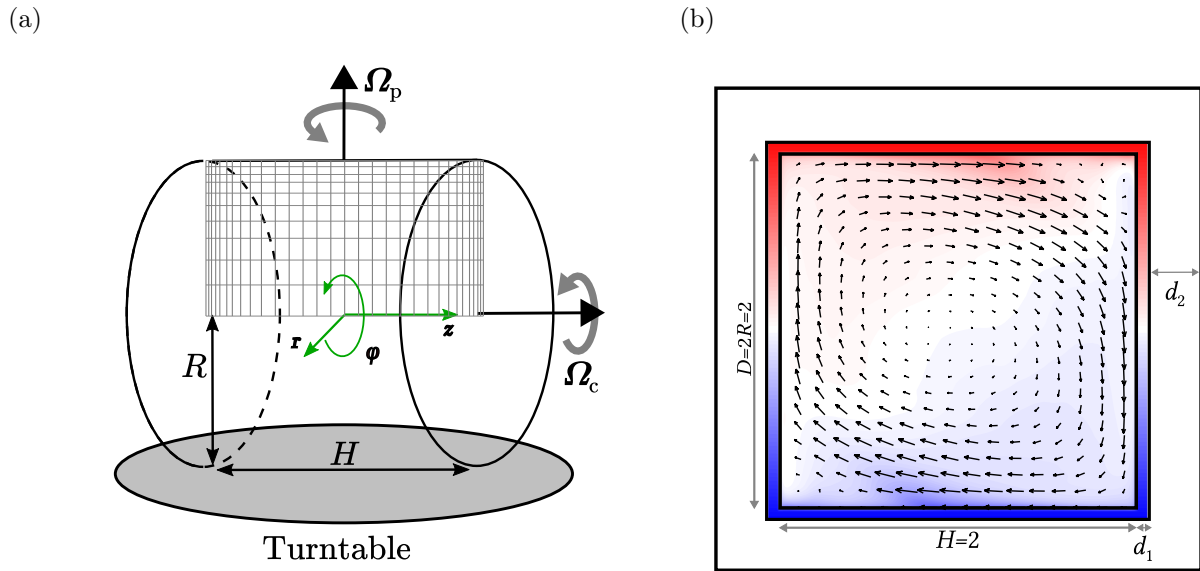


FIG. 1. (a) Sketch of the setup labeling rotation and precession axis. The mesh in the meridional plane shows the spectral elements used for the hydrodynamic models. (b) Geometric setup for the various kinematic models. The inner cylinder with height  $H = 2$  and diameter  $D = 2R = 2$  frames the flow active volume, the intermediate cylinder models the container wall, and the very outer layer represents an outer volume with low electrical conductivity that resembles the laboratory exterior. The colors and the arrows denote a paradigmatic velocity field as applied in the kinematic models.

## B. Boundary conditions and nested outer layers

We estimate the impact of the magnetic boundary conditions employing various setups with one or two outer layers with thickness  $d_1$  and  $d_2$  as sketched in Figure 1b. The underlying idea is that a sufficiently thick outer layer with poor electrical conductivity (large magnetic diffusivity) reduces the impact of the magnetic boundary conditions on the inner volume filled with the electrically conducting fluid. We consider several models that differ in the presence of up to two outer layers with thicknesses  $d_1$  and  $d_2$  that enclose the internal region of the container filled with an electrically conducting fluid (Figure 1b). In all cases, the inner region of the simulation domain consists of a cylindrical container with radius  $R = 1$  and height  $H = 2$  (in dimensionless units) which is filled with an electrically conducting fluid with a magnetic diffusivity  $\eta = 1$ . We examine three different geometric configurations. Initially we revise the results for a setup that considers only the fluid interior (i.e.  $d_1 = 0, d_2 = 0$ ).

The second case examines the impact of a container wall with different values of the magnetic diffusivity (i.e.  $d_1 \neq 0, d_2 = 0, \eta_w = 1 \cdots 8$ ) and two different values for the thickness  $d_1$  of the wall layer. In the thin layer model we use  $d_1 = 0.05$  with a resolution of 5 grid cells and in the thick layer model we use  $d_1 = 0.25$  with a resolution of 25 grid cells, whereby the magnetic diffusivity in the wall layer remains fixed at the maximum value of  $\eta_w = 8$ . As we tackle the problem in the precession frame of reference (with the observer co-rotating with the precession while looking at the spinning container), the wall layer follows a rotational motion with  $u_r = u_z = 0$  and  $u_\varphi = r\Omega_c$ .

Finally, in the fourth model we again apply a thin wall layer with  $d_1 = 0.05$  and  $\eta_w = 8$  surrounded by a second, outer layer with  $d_2 = 0.25$  and  $\eta_o = 8$ , which is supposed to resemble a non-conducting exterior (see Rädler *et al.*<sup>40</sup> and present discussion on page 14). This layer does not co-rotate with the container so that the velocity is set to zero within this layer. At the outer boundaries of the computational domain we apply pseudo-vacuum conditions for the magnetic field, which read  $(\mathbf{B} \times \mathbf{n})_{bc} = 0$ , where  $\mathbf{n}$  is the unit normal vector at the boundary so that the tangential components of the magnetic field at the outer boundary vanish. It is well known that pseudo-vacuum conditions in kinematic models usually underestimate the critical magnetic Reynolds number that must be exceeded for the dynamo to start. The reduction depends on the geometry, i.e. essentially on the aspect ratio, and amounted, for example, to up to 30% in the kinematic models of the VKS dynamo compared to realistic insulator boundary conditions (Giesecke *et al.*<sup>39</sup>).

### C. Velocity field

The fluid flow  $\mathbf{u}$  is prescribed using the data taken from hydrodynamic simulations presented in Pizzi *et al.*<sup>12</sup>, Wilbert, Giesecke, and Grauer<sup>13</sup>, Pizzi, Giesecke, and Stefani<sup>41</sup> and Giesecke *et al.*<sup>14</sup>. In these studies, it was found that the flow in a cylinder emerging at a large nutation angle can be represented by the time-averaged flow with a few large-scale inertial waves that capture the major part of the kinetic energy of the flow. In dependence of the precession ratio defined by  $Po = \Omega_p/\Omega_c$  the flow basically can be characterized by three regimes, which we simply name the subcritical and the supercritical state, and the transition section between both states. A compact representation of the three regimes, which illustrates how the transition between the subcritical state and the

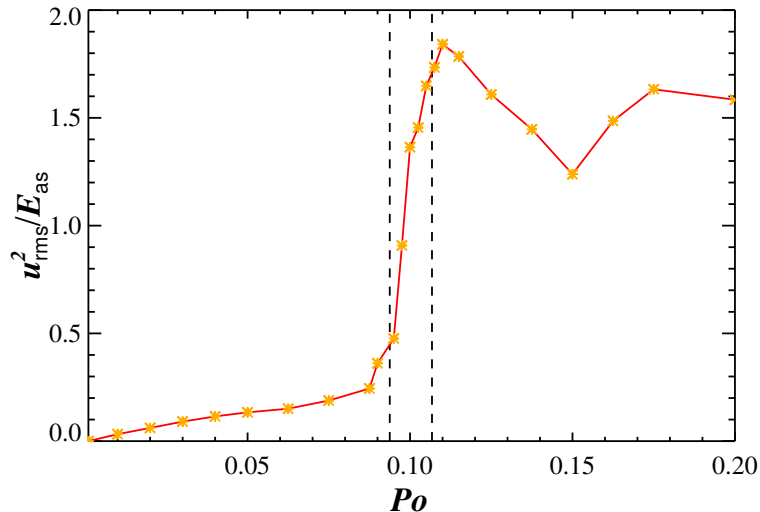


FIG. 2. Root mean square velocity over the kinetic energy of the axisymmetric geostrophic component (circulation) showing the transition from a rotation dominated regime to a non-rotating turbulence.

supercritical state takes place, is provided in Figure 2, which shows the ratio of the energy of the turbulent flow component in the form of the time- and volume-averaged root-mean-square velocity  $u_{\text{rms}}^2 = (\pi R^2 H \Delta T)^{-1} \int |\mathbf{u}(\mathbf{r}, t) - \overline{\mathbf{u}(\mathbf{r})}|^2 dV dt$  to the energy of the actual axisymmetric geostrophic component  $E_{\text{as}} = (\pi H R^2 \Delta T)^{-1} \int |\mathbf{u}^{m=0}(r, z, t)|^2 dV dt$  as a function of  $Po$ . The plot illustrates the abrupt shift from the rotation-dominated regime (below  $Po \approx 0.0925$ ) to the turbulence-dominated regime (above  $Po \approx 0.1075$ ). However, although the fluctuations of the flow with respect to the fluid rotation increase strongly with  $Po$ , the dominant energetic contributions of the precession-induced flow can always be captured by a few large-scale inertial modes, since the significant jump in Figure 2 is determined by both, the increase in turbulence intensity, and the deceleration of the fluid rotation in the core of the cylinder (see Giesecke *et al.*<sup>14</sup>).

The typical structure of the time-averaged flow fields is shown in Figure 3 for three precession ratios  $Po = 0.03, 0.1, 0.2$  that are characteristic for the three flow regimes. In the subcritical state (left column in Figure 3), the flow is essentially laminar, and the geometry can be described by the directly driven flow (first and second row, essentially an  $m = 1$  mode proportional to  $\cos \varphi$ ) and a zonal flow maintained by the cylinder's rotation (geostrophic and axisymmetric, third row). Without precession, this would be a pure solid-body rotation

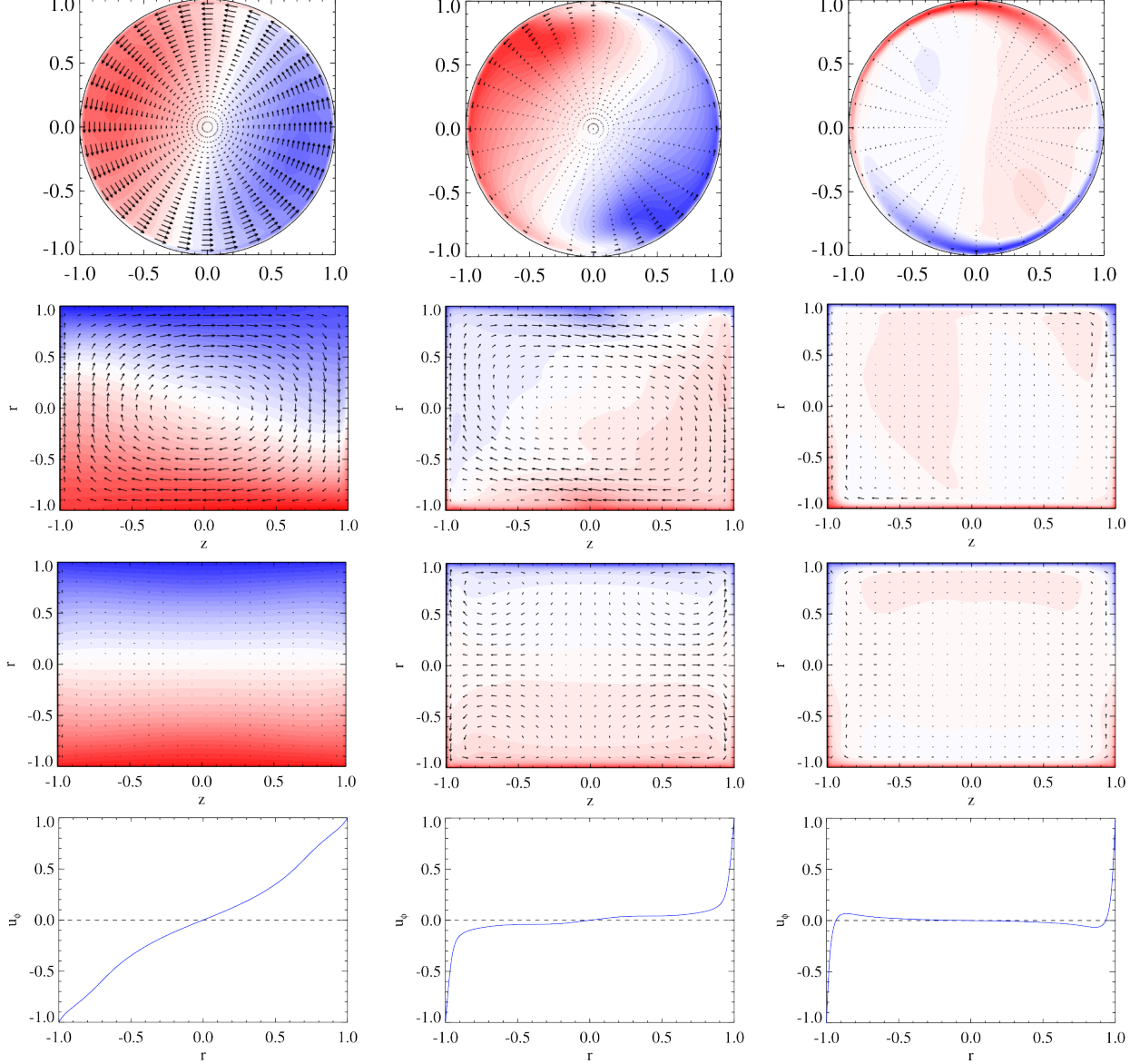


FIG. 3. Characteristic structure of the velocity field for  $\text{Re} = 10^4$  and  $\text{Po} = 0.03, 0.1, 0.2$  (from left to right). From top to bottom: Total flow in the equatorial plane (colors:  $u_z$ , vectors:  $u_r \mathbf{e}_r + u_\varphi \mathbf{e}_\varphi$ ), total flow in the meridional plane where  $u_z$  is maximum (colors:  $u_\varphi$ , vectors:  $u_r \mathbf{e}_r + u_z \mathbf{e}_z$ ), axisymmetric flow (colors:  $u_\varphi$ , vectors:  $u_r \mathbf{e}_r + u_z \mathbf{e}_z$ ), and the radial profile of the axisymmetric angular velocity  $u_\varphi^{m=0}$  in the central plane (at  $z = 0$ ).

$u_\varphi \hat{\mathbf{e}}_\varphi = f(r) \hat{\mathbf{e}}_\varphi$  with  $f(r) = r\Omega_c$  but due to the influence of precession the radial profile  $f(r)$  of the zonal flow is significantly modified (i.e. deceleration of the fluid rotation in the bulk, see bottom row in Figure 3). For larger forcing the flow transients into a supercritical

region, in which the large-scale flow in the inner region almost vanishes so that the fluid essentially performs small-scale turbulent fluctuations and large-scale components are only found near the walls of the container (see right column in Figure 3). These two regimes are linked by a transition zone, which is characterized by an intermittent behavior of the large-scale flow with elements from both regimes. In this transitional region, there exists an additional large-scale contribution in the form of a double roll pattern as shown in the third row of the central column of Figure 3.

This double roll is rather similar to the (time-averaged) poloidal velocity field in the VKS dynamo<sup>1</sup>, and it is well known that such a flow structure generates a dynamo with a relatively low critical magnetic Reynolds number<sup>42</sup> (when also the associated azimuthal flow is taken into account). Indeed, previous kinematic models using a time-averaged flow driven by precession demonstrated that dynamo action is most effective when utilizing the flow obtained in the transitional region between the subcritical and supercritical states<sup>33,34</sup>. A detailed investigation of which components (in terms of inertial modes) are of decisive importance for the dynamo effect was carried out in Giesecke *et al.*<sup>34</sup> and showed that shear adjacent to the side walls plays an important role as well as the presence of the double-roll mode which seems to be responsible for the considerable drop in the critical magnetic Reynolds number.

### III. KINEMATIC GROWTH RATES AND CRITICAL MAGNETIC REYNOLDS NUMBER

#### A. General overview

So far kinematic models for the DRESHDYN dynamo experiment mostly applied pseudo-vacuum conditions for the magnetic field and only few models have been published where an outer wall with finite thickness and with different magnetic diffusivity has been considered<sup>34</sup>. These models indicate that a container wall made of stainless steel, i.e. with a diffusivity that is larger by one order of magnitude when compared to the liquid sodium in the interior, yields growth rates for the magnetic energy similar to the models with pseudo-vacuum conditions. In the following, we will review and deepen these results.

---

<sup>1</sup> In that dynamo experiment the flow was driven by two oppositely rotating disks

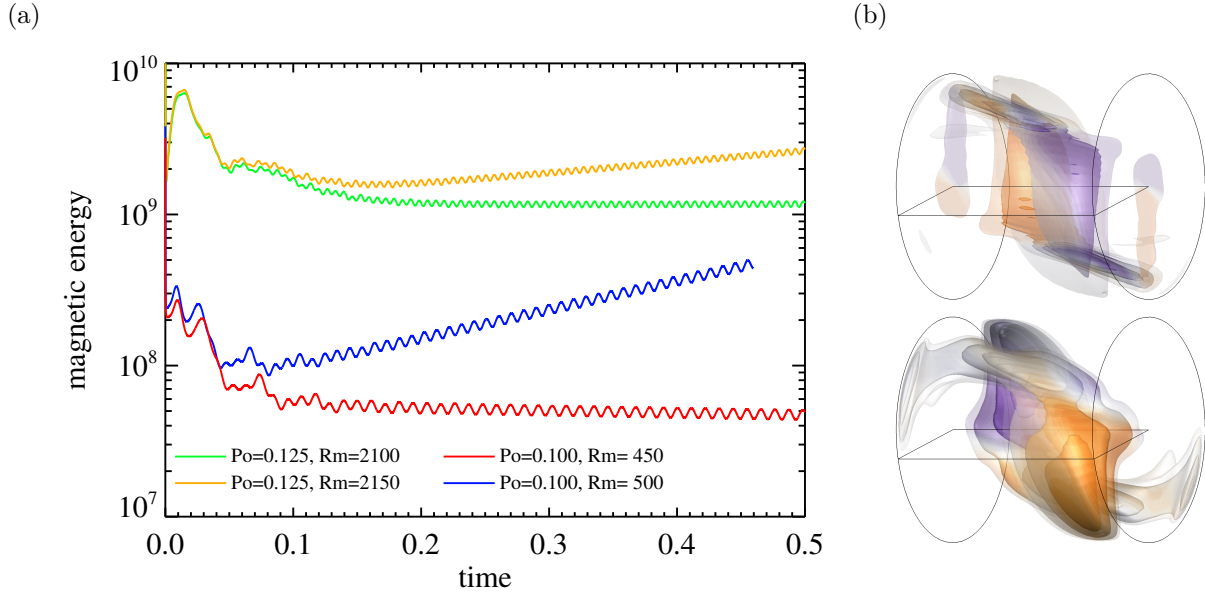


FIG. 4. (a) Magnetic energy versus time for two particular cases with  $Rm = 450$  (red) and  $Rm = 500$  (blue) obtained with the flow field at  $Po = 0.1$  and for  $Rm = 2100$  (green) and  $Rm = 2150$  (orange) obtained with the flow field at  $Po = 0.125$ . (b) Nested iso-surfaces of the magnetic energy at 15%, 30% and 50% of the maximum value for the flow field taken at  $Po = 0.10$ ,  $Rm = 500$  (bottom) and for the flow field taken at  $Po = 0.125$  and  $Rm = 2100$  (top). Both plots are snapshots from an oscillatory state and the corresponding animation movie can be found in the supplemental material of this study<sup>43</sup>.

## B. No layer

The typical behavior of the temporal evolution of the magnetic energy  $E_m = 1/2 \int \mathbf{B}^2 dV$  is shown in Figure 4a. Here we focus on two paradigmatic cases with the flow obtained at  $Po = 0.1$  scaled to a magnetic Reynolds number of  $Rm = 450$  (red curve, decaying solution) and  $Rm = 500$  (blue curve, growing solution), which are slightly below and above the dynamo threshold. A striking feature is the oscillating component of the energy, which is superimposed on the exponentially growing part. For a flow field with a slightly increased  $Po$ , the behavior looks similar in principle, but then a higher magnetic Reynolds number is required for the onset of a dynamo, and the frequency of the oscillating component increases as shown by the orange and green curves in Figure 4a, which result from the flow field

obtained at  $Po = 0.125$ .

The distribution of the magnetic energy looks similar in both cases (see Figure 4b). It is worth mentioning in relation to results including outer boundary layers (see below) that a significant part of the magnetic field energy is observed in the bulk of the cylinder. The temporal dynamics due to the oscillating field component are shown in an animation, which can be found in the supplementary material to this study<sup>43</sup>.

### C. Wall layer

We continue with the setup that considers an additional wall layer with thickness  $d_1 = 0.05$ . Within this layer the magnetic diffusivity  $\eta_w$  is increased in order to emulate the properties of a container wall made of stainless steel. With such an outer layer, we essentially find two new features: (1) the onset for dynamo action is shifted to larger magnetic Reynolds numbers and (2) we can distinguish two different types of dynamo action: if the wall diffusivity is close to that of the fluid (i.e.  $1 < \eta_w \lesssim 2$ ), a dynamo only occurs at very large  $Rm$  ( $Rm^{\text{crit}} > 3500$ ). This dynamo has no oscillatory components (see orange and green curve in Figure 5a) and the associated field energy is concentrated in a narrow region near the end caps (top plot with iso-surfaces in Figure 5b). If the wall layer has an  $\eta_w > 2$  (see red and blue curves in Figure 5a), we obtain an oscillating solution that is similar to the solution in the previous case with pseudo-vacuum boundary conditions. In that case the magnetic field energy is again widely distributed throughout the entire volume with the characteristic pattern shown in the bottom plot of Figure 5b.

A detailed view on the impact of the diffusivity of the outer layer on the growth rates is shown in Figure 6. When the magnetic diffusivity of the outer layer is increased to emulate the effect of a stainless steel container, an eigenmode is excited, the growth rates of which are represented by the inverted parabola in the individual colored curves in Figure 6. For  $\eta_w \gtrsim 2$  this special shape results in positive growth rates at  $Rm$  far below the point where the "regular" curve becomes positive. For further increasing diffusivities the behaviour approaches that of pseudo-vacuum boundary conditions without outer layer (illustrated by the black curve). It is therefore the eigenmode that belongs to the inverse parabolic growth rate, which corresponds to a dynamo that occurs at relatively low  $Rm$  and causes a magnetic field that permeates the entire volume.



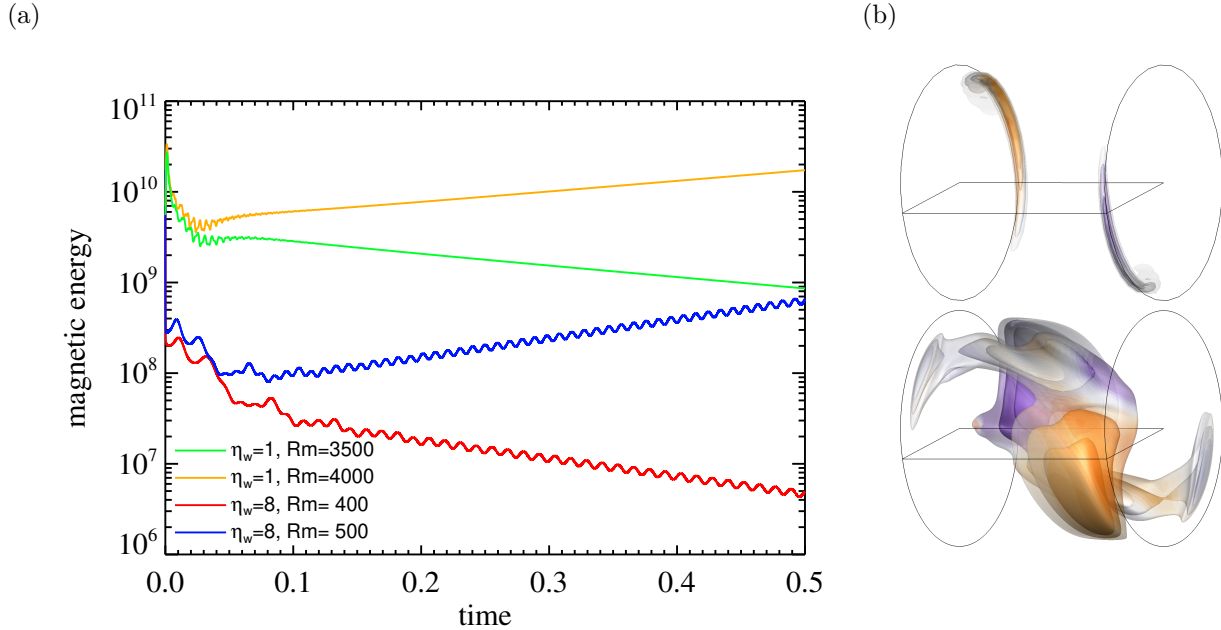


FIG. 5. (a) Magnetic energy versus time for thin outer layer with  $\eta_w = 1$  (same as fluid, green and orange) and  $\eta_w = 8$  (red and blue). In both cases the evolution around the onset of dynamo action is shown for the flow field obtained at  $\text{Po} = 0.1$ . (b) Distribution of magnetic energy for a thin layer solution with  $\eta_w = 1$  and  $\text{Rm} = 4000$  (top) corresponding to the orange curve in plot (a) and for a thin layer with  $\eta_w = 8$  and  $\text{Rm} = 500$  corresponding to the blue curve in plot (a). The nested isosurfaces represent the magnetic energy at 15%, 30% and 50% of the maximum value and the colored mapping denotes the radial field  $B_r$ . Note that the bottom solution exhibits a oscillating behaviour similar to the solutions shown in Figure 4b.

The beneficial effect of the wall layer with (sufficiently) large  $\eta_w$  vanishes, when its thickness  $d_1$  is increased, as shown in Figure 7a which presents the evolution of the magnetic energy for  $d_1 = 0.25$  while the magnetic diffusivity remains at  $\eta_w = 8$ . Here we end up with a critical magnetic Reynolds number slightly above  $\text{Rm}^{\text{crit}} \approx 3000$  and the solution is again characterized by a non-oscillatory behavior with the magnetic energy constraint to two small section close to the endcaps (see Figure 7b), indicating that we are in the low efficiency branch.

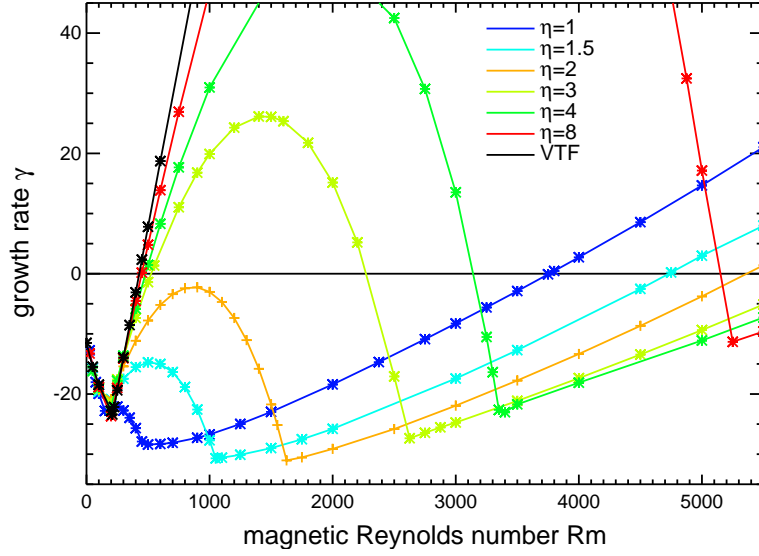


FIG. 6. Growth rates  $\gamma$  of the magnetic field for the time-averaged flow obtained at hydrodynamic simulations at  $\text{Re} = 10^4$  and  $\text{Po} = 0.1$  with various values of the magnetic diffusivity in the thin container walls ( $d_1 = 0.05$ ). The black curve denotes  $\gamma$  for setups with vanishing tangential fields being imposed without container walls ( $d_1 = 0$ ).

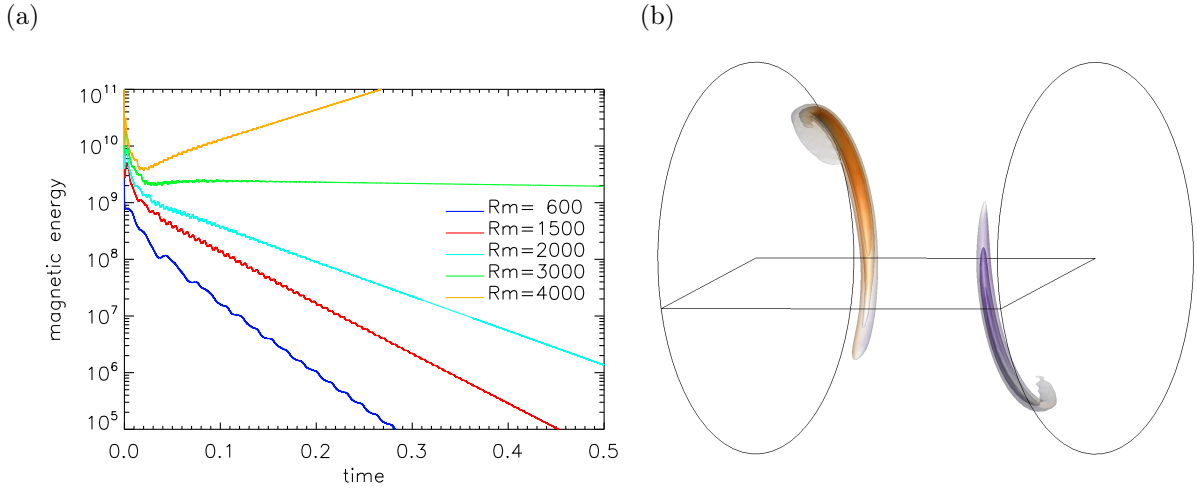


FIG. 7. (a) Magnetic energy versus time for the setup with thick container wall ( $d_1 = 0.25, d_2 = 0$ ). (b) isosurfaces for thick layer with  $\eta_w = 8, \text{Rm} = 3000$  (green curve in (a)),

## D. Wall layer plus outer layer

The high-efficient branch can also be achieved by assuming a configuration, where the container wall is emulated by a thin co-rotating layer with  $d_1 = 0.05$ , while the exterior domain is modeled by a thick resting outer layer with  $d_2 = 0.25$ . Here both additional layers have the same diffusivity, i.e.  $\eta_w = \eta_o = 8$  (actually, since the thick outer layer emulates the exterior this should be an insulator with  $\eta_o \rightarrow \infty$ ). In this case, we again obtain an oscillating solution that occupies the entire cylinder volume (see Figure 8) and has a similar structure as in the case of the thin layer or pseudo-vacuum boundary conditions without an outer layer shown in Figures 4 and 5. However, the critical magnetic Reynolds number of  $Rm^{\text{crit}} \approx 1350$  is now about two and a half times as large as in the previous cases and the amplitude of the oscillating part remains rather small.

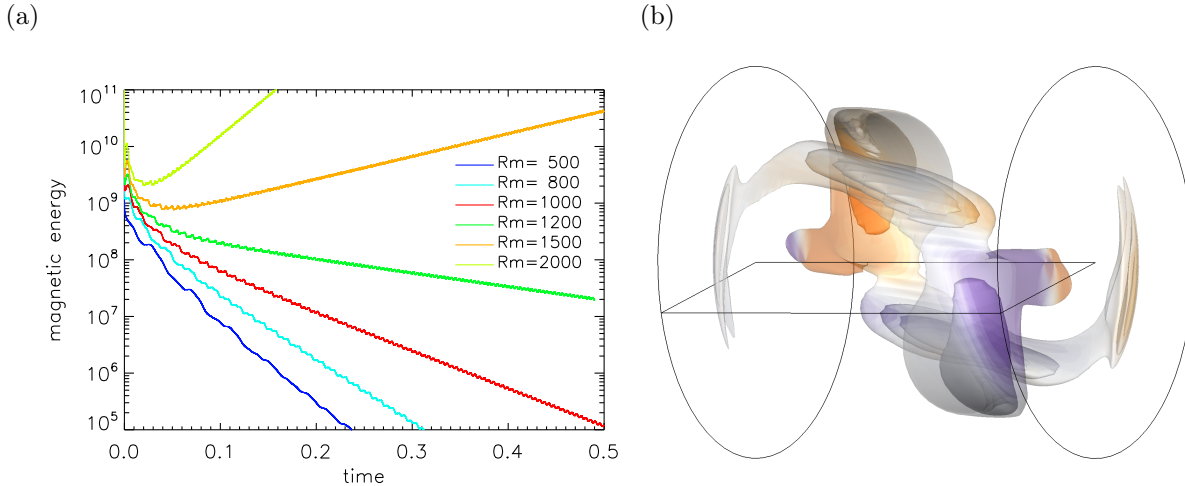


FIG. 8. (a) Magnetic energy versus time for the setup with thin outer wall and stagnant outer layer ( $d_1 = 0.05, d_2 = 0.25$ ) and (b) thin wall with  $\eta_w = 8, Rm = 1500$ , outer resting layer (orange curve in (a)).

## E. Impact of the structure of the velocity field

In the following we focus on the setup with wall layer and outer layer for which we applied various time averaged velocity fields obtained within the interval  $0.0875 \leq Po \leq 0.11$ . It is known from the hydrodynamic investigations that the structure of the velocity field changes

only slightly within the transition between subcritical and supercritical state. Nevertheless, these gradual changes are sufficient to cause a variation in the critical magnetic Reynolds number, especially at the borders of the transition region. Figure 9 shows the growth rates for the model with wall and outer layers but varying the flow structure by using time-averaged flow fields obtained at different  $Po$ . Similar to the results with wall layer only (Figure 6), we see a behavior for some velocity fields that can be described by an inverse parabola, at least around the range with positive growth rates. This does not apply to velocity fields with  $Po \leq 0.0925$  or with  $Po \geq 0.1075$ . For these parameters, the parabolic behavior does not occur, and positive growth rates are found - if at all - for very large  $Rm$ .

The intersection of the growth rates with the abscissa reveals the critical magnetic Reynolds number required for the onset of a dynamo. Figure 10 shows this number as a function of  $Po$  for two different setups. The blue curve shows  $Rm^{\text{crit}}$  for the original setup without any outer layer. The most outstanding feature of the blue curve is the reduction of the critical magnetic Reynolds number in the range  $0.095 \lesssim Po \lesssim 0.11$  with the lowest value being  $Rm^{\text{crit}} \approx 450$ , obtained for the flow field from hydrodynamic simulations at  $Po = 0.1$ . Below  $Po = 0.0925$  no more dynamos were found, while above  $Po = 0.11$  the critical magnetic

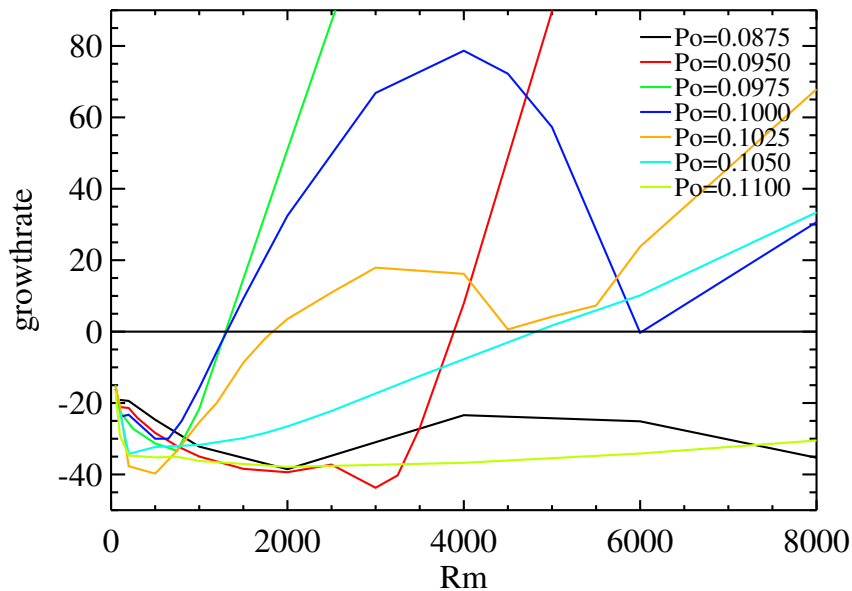


FIG. 9. Growth rates for the setup with wall layer and outer layer for various realisations of the velocity field obtained at different  $Po$ .

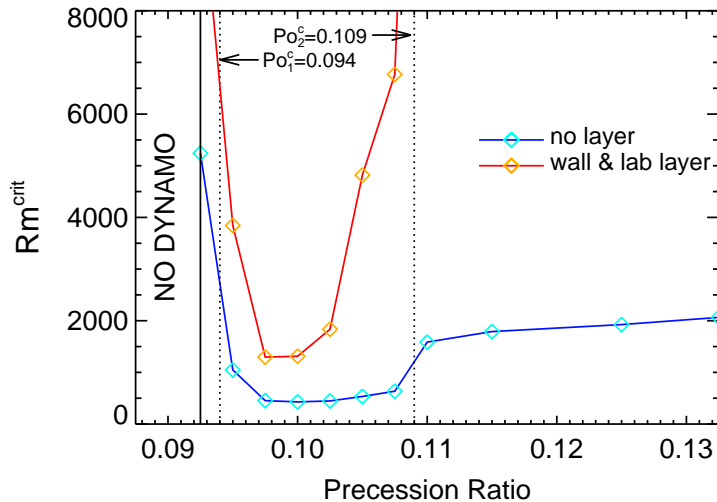


FIG. 10. Critical magnetic Reynolds number required for the onset of dynamo action using time-averaged flow fields from hydrodynamic simulations at  $\text{Re} = 10^4$ . The dotted vertical lines denote the transitional section (with a significant contribution of the double-roll mode). The blue curve shows the case  $d_1 = 0$  (no layer) and the red curve shows the case  $d_1 = 0.05, d_2 = 0.25$  (2 outer layers).

Reynolds number is in the range of about  $\text{Rm}^{\text{crit}} \approx 2000$ . The region  $0.095 \lesssim \text{Po} \lesssim 0.11$  coincides exactly with the transition region from the subcritical to the supercritical state of the velocity field, and we therefore assume that the axially symmetric double roll occurring exclusively in this parameter range plays a significant role for the onset of dynamo action at comparatively small magnetic Reynolds numbers (see Giesecke *et al.*<sup>34</sup>).

This behaviour changes, when considering the case with two outer layers that is represented by the red curve in Figure 10. In these models the onset for dynamo action is shifted to larger magnetic Reynolds numbers so that the minimum is now  $\text{Rm}^c \approx 1300$  which is found for the flow field obtained at  $\text{Po} = 0.0975$ . Furthermore, the range of flow fields with a (relatively) small critical magnetic Reynolds number narrows and only spans the interval  $0.095 \lesssim \text{Po} \lesssim 0.105$ . Interestingly, although we still use the same structure for the flow fields, we get a large  $\text{Rm}^c$  even when the double roll mode is present with a significant amplitude. This indicates that the impact of the double roll mode might be less significant than expected from the cases without outer layers but that the electromagnetic coupling of the field induced essentially by shear close to the fluid boundary layers with the side walls

with finite electrical conductivity has a similarly large influence.

#### IV. FULL SET OF MAGNETOHYDRODYNAMIC EQUATIONS

In the following we present results obtained from the simulation of the induction equation coupled with the Navier-Stokes equation in a self-consistent MHD model.

##### A. Code scheme

The full magnetohydrodynamic problem additionally requires a computation of the temporal evolution of the flow field. In this case, the Navier-Stokes equation needs to be solved as well, which for a precessing flow in the rotating frame of reference takes the form

$$\frac{\partial \mathbf{u}}{\partial t} = -\mathbf{u} \cdot \nabla \mathbf{u} - \nabla p + \frac{1}{\text{Re}} \Delta \mathbf{u} - 2(\text{Po} \mathbf{k}_p \times \hat{\mathbf{z}}) + (\nabla \times \mathbf{B}) \times \mathbf{B} + \text{Po} \sin \alpha r \cos(\varphi + t) \hat{\mathbf{z}}. \quad (2)$$

In addition to the terms commonly encountered in regular flow problems describing nonlinear interactions and dissipation, we have three additional contributions: the Coriolis force due to rotation, the Lorentz force due to the interaction with the magnetic field, and the Poincaré force accounting for acceleration due to perpetual change of the orientation of the cylinder's axis of rotation. A detailed derivation of the Navier-Stokes equation for a precessing system is given e.g. in Tilgner<sup>28</sup>.

We conduct direct numerical simulations (DNS) of the coupled system of equations (1) and (2) using the code `SpecDyn`<sup>13,44</sup>, which is based on a pseudo-spectral Fourier approach. The drawback of this approach is the requirement of periodic boundary conditions in all three directions. Since this rules out an application of a closed cylindrical geometry, the scheme is complemented by a direct forcing immersed boundary method (IBM) which allows the consideration of nearly arbitrary shaped boundaries that prescribe the confinement for the fluid flow when the boundary conditions on these boundaries are of no-slip type. The fulfilment of the divergence-free condition for the velocity field is ensured using a Pressure-Corrector method. The same scheme is also applied to the magnetic field to ensure that the solution of the induction equation is divergence-free as required by Maxwell's equations. The code is parallelized using a two-dimensional processor grid. To apply the Fast Fourier Transform (FFT) to the distributed data along all spatial directions, the processor grid must be

transposed, which is achieved by leveraging advanced MPI functions to perform an all-to-all communication of the processor data. Tests have been conducted with various configurations that proved accurate solutions with excellent convergence properties and nearly perfect strong scaling properties. A detailed description is given in Wilbert, Giesecke, and Grauer<sup>13</sup> and in Wilbert<sup>44</sup> and a comparable approach was used for numerical models of the VKS dynamo<sup>45,46</sup>.

## B. Model set-up

We consider a setup comparable to the kinematic models with a stagnant outer layer, i.e. a setup given by a cylindrical fluid region with radius  $R = 1$  and height  $H = 2$  embedded in a Cartesian domain with a edge length  $L = 3$  so that the size of the box provides sufficient space to let the magnetic field decline outside the cylindrical vessel. The cylindrical vessel is implemented by imposing internal conditions on the fluid that emulate the (virtual) container walls by enforcing no-slip conditions at the surface of the container. Unlike in the kinematic (multi-)layer models we do not model any special region representing the wall of the vessel because such a layer would not be properly resolved. Instead we use a magnetic diffusivity  $\eta = 1$  for the fluid region, whereas the 'non-liquid' region outside the vessel has a magnetic diffusivity  $\eta_e = 10$ , which is supposed to emulate an electrically isolating exterior. All simulations are carried out with a Reynolds number  $\text{Re} = \Omega_c R^2 / \nu = 6400$  which is the maximum possible at the resolution of  $N = 256^3$  while still sufficiently resolving the boundary layers at the fluid-wall interface of the vessel<sup>44</sup>.

## C. Results

Similar to the procedure in the kinematic case, we vary the Poincaré number  $\text{Po}$ , whereby different magnetic Reynolds numbers are considered, beginning with high values. If a positive mean growth rate is found for a particular set of parameters, further runs are executed consecutively lowering the value of  $\text{Rm}$  until no more dynamo action can be observed. Similar to the kinematic models we find a limited range for the preferred occurrence of a dynamo in the interval  $0.105 \lesssim \text{Po} \lesssim 0.125$ . However, the critical magnetic Reynolds number is significantly higher with a minimum value of  $\text{Rm}^{\text{crit}} \approx 5600$  at  $\text{Po} = 0.11$ . The slightly

larger value for the optimum Po compared to the kinematic models can be explained by the (slightly) smaller Re (see also Giesecke *et al.*<sup>14</sup>). In the following we focus on the particular case Po = 0.11 and Rm = 6500 and compare the properties of this DNS solution with the results found in the kinematic case. The chosen paradigmatic example well characterizes the DNS solutions found very close to the threshold while allowing a faster growth with shorter time period until a statistically steady state is reached.

### 1. Temporal evolution of the kinetic energy

The temporal evolutions of kinetic and magnetic energy  $E_k$  and  $E_m$  are displayed in Fig. 11, where  $E_k$  and  $E_m$  are defined as

$$E_k = \frac{1}{2L^3} \int_{L^3} |\mathbf{U}(\mathbf{r}, t)|^2 dV, \text{ and } E_m(t) = \frac{1}{2L^3} \int_{L^3} |\mathbf{B}(\mathbf{r}, t)|^2 dV \quad (3)$$

and where  $L$  denotes the edge length of the cubic domain. The simulations start with the pure hydrodynamic case, which is processed until a quasi-stationary statistically steady state is reached. A detailed description of the hydrodynamic behavior is given in Wilbert, Giesecke, and Grauer<sup>13</sup>. Here we focus on the properties of the magnetic field in the dynamo case and the resulting feedback on the velocity field. After switching on the magnetic induction at  $t = 300$ , the magnetic energy begins to grow for about 100 cylinder rotations and finally goes into saturation. Both, kinetic and magnetic energy are dominated by contributions of the azimuthal components of the related field. However, the dominance for the magnetic field is not particularly pronounced and the induced magnetic energy  $E_m$  remains much smaller than  $E_k$ . We find that, even in the saturated state, the presence of the magnetic field does not substantially alter the structure and the amplitude of the fluid flow via the Lorentz force. A striking property of the magnetic energy is that, unlike the kinetic energy, which remains relatively steady, the magnetic energy is characterized by strong occasional peaks where  $E_m$  suddenly rises 3 to 5 times above its average value. There are no related substantial changes in the flow field due to the back-reaction of the magnetic field so that the bursts can be clearly assigned to corresponding peaks in the interaction parameter  $\zeta$ , which compares the amplitude of the Lorentz force to the inertial term in the Navier-Stokes equation:

$$\zeta = \frac{|(\nabla \times \mathbf{B}) \times \mathbf{B}|}{|\mu_0(\mathbf{u} \cdot \nabla)\mathbf{u}|}. \quad (4)$$



For a self-excited dynamo  $\zeta$  follows  $\sim B^2/U^2$  (see Miralles, Plihon, and Pinton<sup>48</sup>), which is indeed the case as shown in Figure 12, where we see similar irregular peaks due to the bursts shown by the magnetic energy in Figure 11b. However, the impact of the magnetic field remains small even in the case of a burst.

In the following, we discuss three characteristic periods as labeled by capital letters A, B, (two paradigmatic peaks) and C (quiescent period) in Figure 12. Figure 13 shows three rows each with four snapshots of the spatial distribution of the magnetic energy taken at four arbitrary times within each related period. Animated sequences showing the time development within the marked periods can be found in the supplementary material of this study<sup>47</sup>. We recognize a small scale field formed by flux patches distributed randomly in space and time. These patches are short-lived despite the strong concentration of magnetic energy, and even if they appear regularly, no corresponding period can be assigned. The magnetic field patches are slightly elongated in the azimuthal direction and during a typical peak period, we see an increased excitation of medium-scale concentrations of magnetic energy in terms of elongated arc-like magnetic structures near the end caps (Figure 13a–13h). However, these mid-scale magnetic field structures remain isolated and decay within 1–2 rotation periods, whereby the resulting small scale patches have a rather isotropic character and are distributed within the entire volume of the cylinder. While the distribution of the

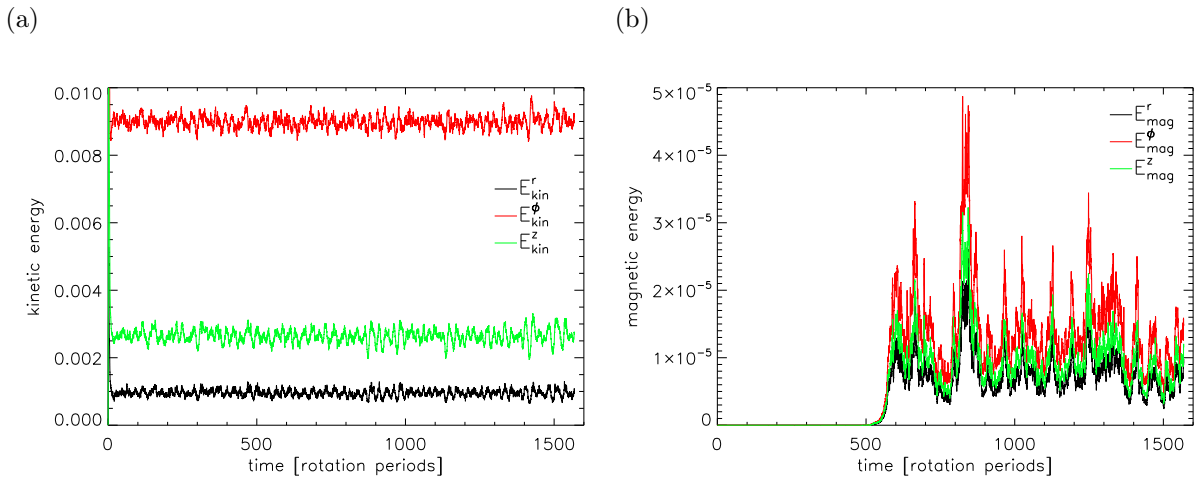


FIG. 11. Temporal evolutions of the kinetic (a) and magnetic (b) energy for  $\text{Re} = 6400$ ,  $\text{Rm} = 6500$  and  $\text{Po} = 0.11$ .

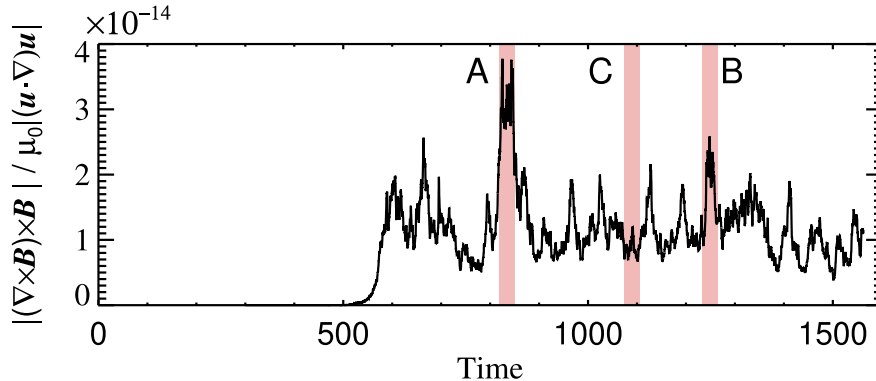


FIG. 12. Interaction parameter showing the bursts of magnetic energy in comparison with the kinetic energy. The vertical lines mark the time steps as visualized in Figure 13 and the shaded area shows the period for which animations are available in the supplementary data of this study<sup>47</sup>.

magnetic energy in individual snapshots appears to be largely chaotic (with the exception of the bursts), this is no longer the case when we look at the time average in the turntable system. Applying a long averaging time of more than 200 rotation periods, we obtain a rather regular distribution of magnetic energy as shown in Figure 14. Similar to the low-efficient branch of the kinematic models we find elongated structures close to the end caps, which are a result of the statistical distribution of the magnetic field energy. Furthermore, and in contrast to the kinematic models, we recognize different symmetries with respect to the mid-plane of the cylinder, which are expressed in the different signs for the time-averaged radial field. We therefore see both, a dipole-like state and a quadrupole-like state, which are alternately dominant at irregular intervals. Due to the small-scale structure, however, the characterization as a dipole or quadrupole field is not really justified. In this sense, the results are consistent with other dynamo simulations in which a mechanical forcing was utilized as driving mechanism (see e.g. Lin *et al.*<sup>49</sup>, Cébron *et al.*<sup>5</sup>, Reddy, Favier, and Le Bars<sup>50</sup>). In agreement with Landeau’s conclusions<sup>9</sup>, we therefore confirm that it remains unclear whether mechanical forcing can generate a large-scale magnetic field, and apart from experimental investigation, only simulations with massively reduced viscosity (i.e. massively larger Reynolds number) can help to clarify this question, which is currently prevented by insufficient performance of numerical algorithms and HPC systems.

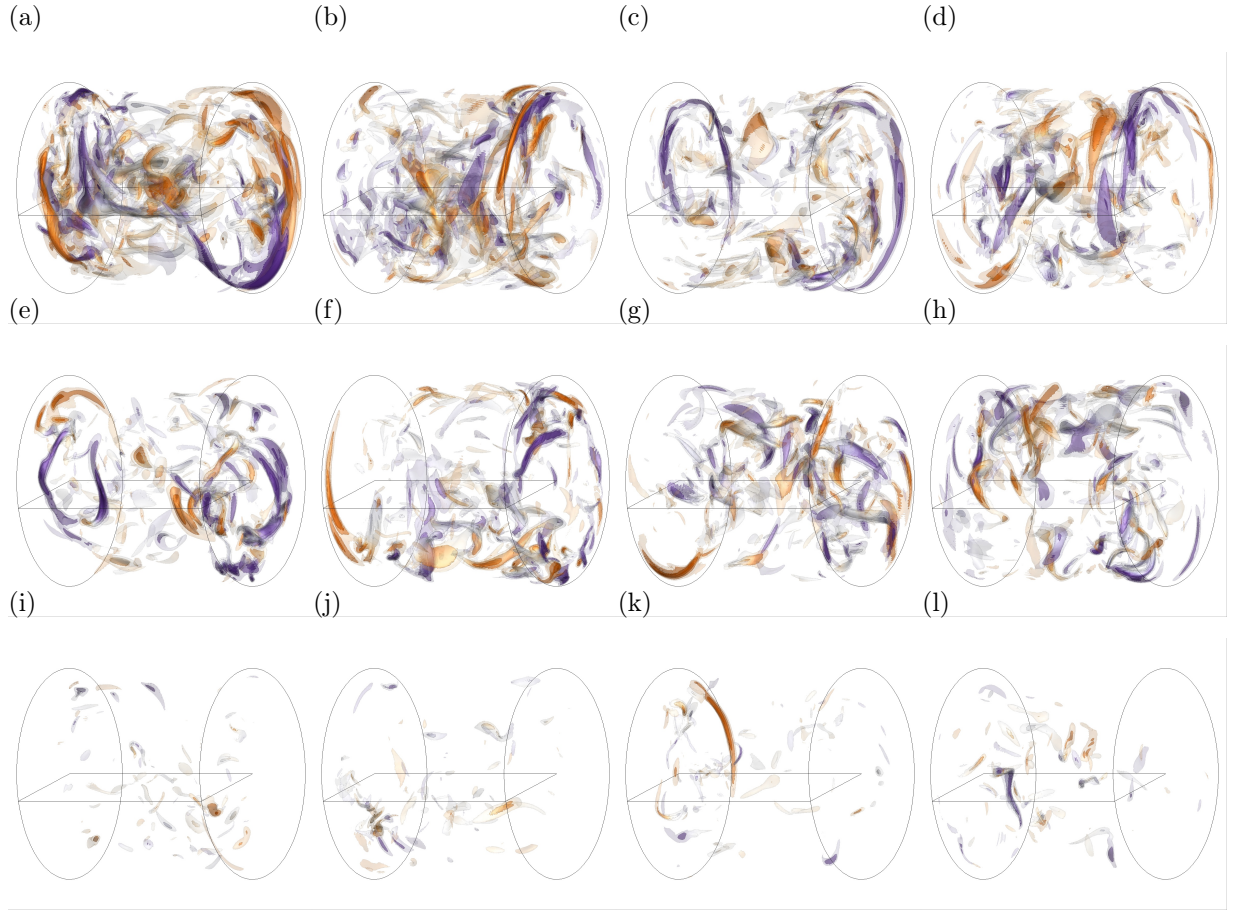


FIG. 13. Snapshot of the magnetic energy at 5%, 15%, 30%, and 50% of the respective average value. Each row presents four arbitrary snapshots taken within the related period  $A$ ,  $B$ , and  $C$  (from top to bottom). The color codes represent the radial component of the magnetic field.

## 2. *Back-reaction and kinetic power spectrum*

In contrast to the magnetic field, the velocity field is always dominated by large scales as shown in Figure 15 by means of a paradigmatic time-snapshot of the three-dimensional distribution of the axial velocity component  $u_z$ . This figure shows the typical structure of the velocity, which looks very similar at any time, regardless of whether with or without a magnetic field, or whether within a peak period or within a magnetically quiet section. Indeed, a reduction of the speed amplitude and/or of the field structure is not absolutely necessary, because here we deal with a small-scale dynamo for which theoretical considerations (in a mean-field model) have shown that the feedback via the Lorentz force can be described by an increased diffusivity or hyperdiffusivity  $\propto \nabla^4 \mathbf{B}$  (Subramanian<sup>51</sup>). A

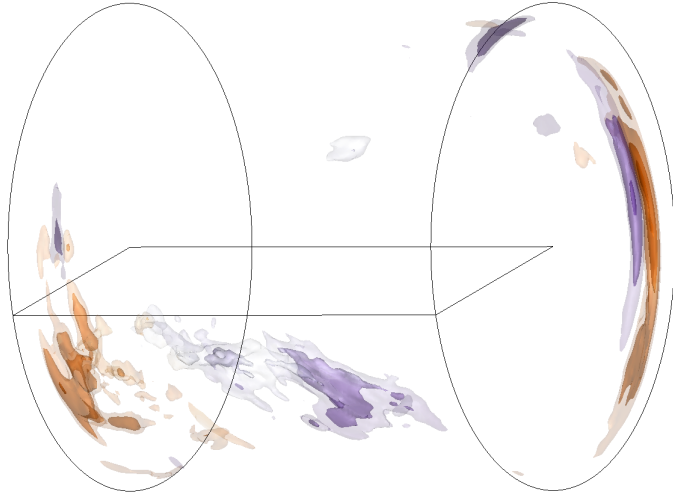


FIG. 14. Time averaged iso-surfaces of the magnetic energy. The colors denote the radial magnetic field component.

response of the fluid flow can be seen in a subtle way when looking at the temporal power-spectra of kinetic energy. Figure 16 compares the temporal power spectrum of the kinetic energy for the hydrodynamic case (left panel) with the spectrum for the dynamo case (right panel). Here we assume that in the high frequency range the kinetic energy of the individual components  $r, \varphi$  and  $z$  scales according  $\hat{E}_k \propto \nu^\alpha$  where  $\hat{E}_k$  is the energy from the Fourier component with the frequency  $\nu$  and  $\alpha$  is a spectral index that turns out to be different for the horizontal coordinates ( $r, \varphi \rightarrow \alpha_\perp$ ) and the vertical coordinate ( $z \rightarrow \alpha_\parallel$ ). In the hydrodynamic case, the contributions to high frequencies by the axial component  $z$  (spectral index  $\alpha_\parallel = -2.9$ ) drop significantly faster than the contributions of the horizontal components  $r$  and  $\varphi$  (spectral index  $\alpha_\perp \approx -1.8$ ). In the dynamo case, the spectral index of the horizontal components approaches  $\alpha_\perp \approx -2.5$  which is close to the axial component, which practically does not change compared to the hydrodynamic case. In summary, in the magnetic case we find an isotropization of the spectrum and a damping of the temporal fluctuations, which is expressed in the steeper spectrum.

## V. SUMMARY AND CONCLUSIONS

We have run numerical simulations of precession driven dynamo action in a cylindrical cavity. We examined simplified kinematic models as well as a particular setup of a similar

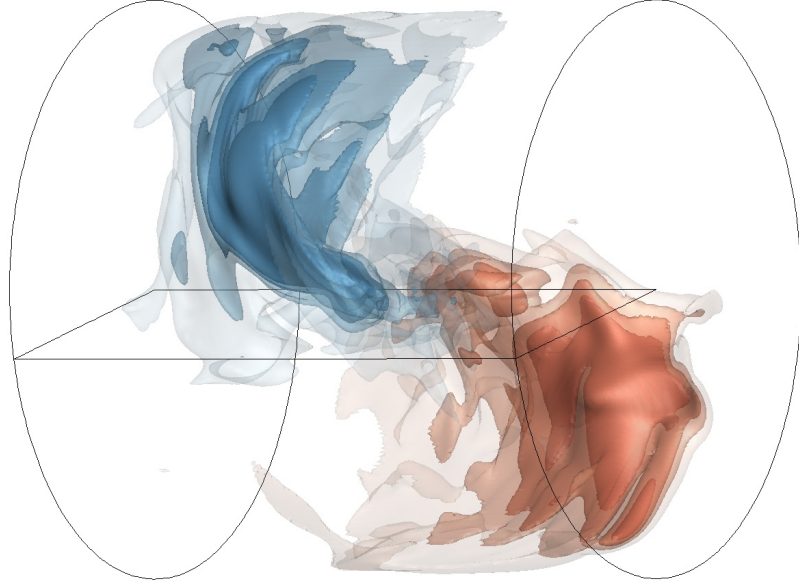


FIG. 15. Snapshot of the axial velocity at an arbitrary timestep during the first peak A. The velocity field looks rather similar independently of being at a peak state or in the quiescent region. An animations of the axial component shown in this plot can be found in the supplementary material.

system solved by a self-consistent three-dimensional magnetohydrodynamic approach. The kinematic models reveal the existence of two different branches for dynamo action, the realization of which depends on the configuration of the outer boundary regions. The first branch is characterized by a highly localized and stationary dynamo that only occurs at

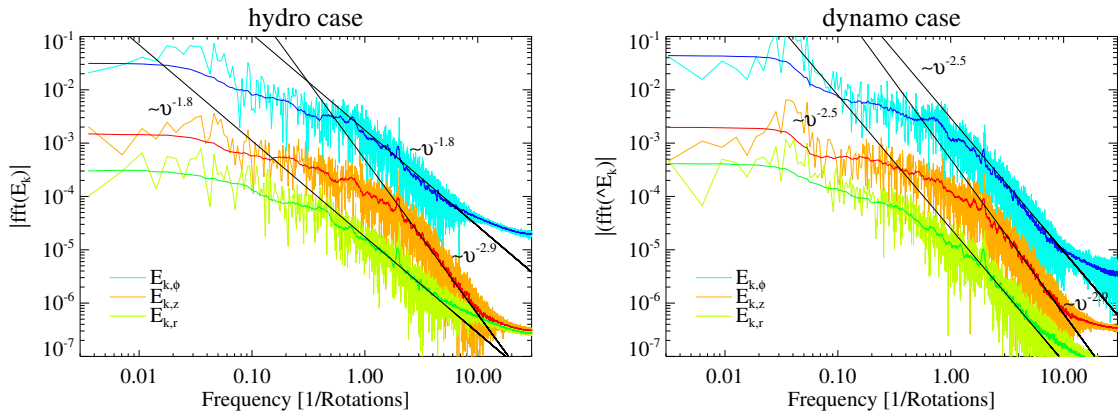


FIG. 16. Temporal power spectrum of the velocity field in the hydro case (a) and in the dynamo case (b).

rather large magnetic Reynolds number. The second type of dynamo is of oscillatory type with the magnetic field filling a larger proportion of the fluid domain. This type can occur at much lower magnetic Reynolds number, which, however requires suitable boundary conditions in terms of either a thin outer layer with large magnetic diffusivity or a comparable emulsion with pseudo-vacuum BC.

We have not investigated here at which exact parameters the transition from one branch to the other takes place, since the experimental realization must in any case start from a basically infinitely large outer volume of an insulator, namely the air in the laboratory. The kinematic model with two outer layers (for the container walls and for the lab environment), which we assume best reflects the experimental setup, has a critical magnetic Reynolds number of  $Rm_{\text{crit}} \approx 1300$ , which agrees surprisingly well with the value derived by Goepfert and Tilgner<sup>30</sup> obtained from simulations in a precessing cube. Our solutions with external outer walls and an increased diffusivity (i.e. a decreased electrical conductivity) are consistent with previous studies<sup>52,53</sup>, who found a monotonic reduction of the dynamo threshold for increasing conductivity of an outer wall. Furthermore, these studies also reported a reduction for oscillatory solutions with an optimum at a particular thickness of the outer wall, which was explained by the increased dissipation resulting from eddy currents induced in the outer wall.

We also used direct numerical simulations in order to investigate the time evolution of the velocity field, the impact of the magnetic field through the Lorentz force and the consistency with the kinematic models. Unfortunately, it is not possible to achieve the large hydrodynamic Reynolds number, as it is relevant in the experiment, due to the limitations of the numerics and the hardware, so that we find dynamo solutions in the DNS only for relatively large magnetic Reynolds numbers. This means that we effectively deal with a magnetic Prandtl number of the order of one and that the magnetic field is of small-scale type. At this stage it cannot be concluded with certainty that this behavior will change if we move to larger (hydrodynamic) Reynolds numbers, as there are currently insufficient parameter studies available for such scaling. Nevertheless, for the parameters considered, a small-scale burst dynamo is the typical solution. These bursts are characterized by peaks in magnetic energy, which represent the sudden excitation of large-scale magnetic field structures. Since these structures are isolated and not sustained throughout the entire volume, they are rapidly destroyed by magnetic diffusion. Our results align with findings obtained for exam-

ple by Etchevest, Fontana, and Dmitruk<sup>54</sup>, Richardson, Hollerbach, and Proctor<sup>55</sup>, Hughes, Cattaneo, and Thelen<sup>56</sup>, which conclude that increasing the magnetic Prandtl number leads to a transition from large-scale dynamos to small-scale dynamos.

The small scale characteristics of the magnetic fields from the DNS are clearly different from the properties of the field obtained in the kinematic simulations. However, if the magnetic field from the DNS is averaged over a sufficiently long period of time so that the occasional occurrence of the strongly localized patches is also averaged out, the structure is comparable to the structure of the weakly efficient branch in the kinematic models, which only appears at large magnetic Reynolds numbers. This explains, at least in part, the high magnetic Reynolds number required to obtain a dynamo in the DNS.

In order to obtain a dynamo solution that can also be realized in the planned experiment, it would be necessary to find a path that leads to the efficient dynamo branch with low  $Rm^c$ . Whether this exists at all in the full MHD case, and how this can be achieved, remains unknown at present.

## ACKNOWLEDGMENTS

This work benefited from support through Project Nos. GR 967/7-1 and GI 1405/1-1 of the Deutsche Forschungsgesellschaft (DFG). The authors gratefully acknowledge the Gauss Centre for Supercomputing e.V. ([www.gauss-centre.eu](http://www.gauss-centre.eu)) for funding this project by providing computing time through the John von Neumann Institute for Computing (NIC) on the GCS Supercomputer JUWELS at Jülich Supercomputing Centre (JSC). Ján Šimkanin is grateful for support from the Alexander-von-Humboldt Stiftung (CZE 1079936) and for funding from the Helmholtz Association in frame of the AI project GEOMAGFOR (ZT-I-PF-5-200).

## REFERENCES

- <sup>1</sup>R. Stieglitz and U. Müller, “Experimental demonstration of a homogeneous two-scale dynamo,” *Phys. Fluids* **13**, 561–564 (2001).
- <sup>2</sup>A. Gailitis, O. Lielausis, S. Dement’ev, E. Platadis, A. Cifersons, G. Gerbeth, T. Gundrum, F. Stefani, M. Christen, H. Hänel, and G. Will, “Detection of a Flow Induced Magnetic Field Eigenmode in the Riga Dynamo Facility,” *Phys. Rev. Lett.* **84**, 4365–4368 (2000).



- <sup>3</sup>R. Monchaux, M. Berhanu, M. Bourgoïn, M. Moulin, P. Odier, J.-F. Pinton, R. Volk, S. Fauve, N. Mordant, F. Pétrélis, A. Chiffaudel, F. Daviaud, B. Dubrulle, C. Gasquet, L. Marié, and F. Ravelet, “Generation of a Magnetic Field by Dynamo Action in a Turbulent Flow of Liquid Sodium,” *Phys. Rev. Lett.* **98**, 044502 (2007), [10.1103/PhysRevLett.98.044502](#).
- <sup>4</sup>F. Stefani, T. Albrecht, G. Gerbeth, A. Giesecke, T. Gundrum, J. Herault, C. Nore, and C. Steglich, “Towards a precession driven dynamo experiment,” *Magnetohydrodynamics* **51**, 275–284 (2015).
- <sup>5</sup>D. Cébron, R. Laguerre, J. Noir, and N. Schaeffer, “Precessing spherical shells: flows, dissipation, dynamo and the lunar core,” *Geophys. J. Int.* **219**, S34–S57 (2019).
- <sup>6</sup>W. V. R. Malkus, “Precession of the Earth as the Cause of Geomagnetism,” *Science* **160**, 259–264 (1968).
- <sup>7</sup>C. Stys and M. Dumberry, “A past Lunar dynamo thermally driven by the precession of its inner core,” *Journal of Geophysical Research: Planets* **125**, e2020JE006396 (2020).
- <sup>8</sup>P. Olson, “The new core paradox,” *Science* **431–432**, 013008 (2013).
- <sup>9</sup>M. Landeau, A. Fournier, H.-C. Nataf, D. Cébron, and N. Schaeffer, “Sustaining earth’s magnetic dynamo,” *Nature Reviews Earth and Environment* **3**, 255 – 269 (2022).
- <sup>10</sup>M. G. Rochester, J. A. Jacobs, D. E. Smylie, and K. F. Chong, “Can precession power the geomagnetic dynamo?” *Geophys. Journal* **43**, 661–678 (1975).
- <sup>11</sup>R. R. Kerswell, “Upper bounds on the energy dissipation in turbulent precession,” *J. Fluids Mech.* **321**, 335–370 (1996).
- <sup>12</sup>F. Pizzi, A. Giesecke, J. Šimkanin, and F. Stefani, “Prograde and retrograde precession of a fluid -filled cylinder,” *New J. Phys.* **23**, 123016 (2021).
- <sup>13</sup>M. Wilbert, A. Giesecke, and R. Grauer, “Numerical investigation of the flow inside a precession-driven cylindrical cavity with additional baffles using an immersed boundary method,” *Phys. Fluids* **34**, 096607 (2022).
- <sup>14</sup>A. Giesecke, T. Vogt, F. Pizzi, V. Kumar, F. Garcia-Gonzalez, T. Gundrum, and F. Stefani, “The global flow state in a precessing cylinder.” *J. Fluid Mech.* **998**, A30 (2024).
- <sup>15</sup>J. J. Kobine, “Azimuthal flow associated with inertial wave resonance in a precessing cylinder,” *J. Fluid Mech.* **319**, 387 – 406 (1996).
- <sup>16</sup>R. Manasseh, “Breakdown regimes of inertia waves in a precessing cylinder,” *J. Fluids Mech.* **243**, 261–296 (1992).



- <sup>17</sup>R. Manasseh, “Distortions of inertia waves in a rotating fluid cylinder forced near its fundamental mode resonance,” *J. Fluids Mech.* **265**, 345–370 (1994).
- <sup>18</sup>R. Manasseh, “Nonlinear behaviour of contained inertia waves,” *J. Fluids Mech.* **315**, 151–173 (1996).
- <sup>19</sup>J. Noir, D. Brito, K. Aldridge, and P. Cardin, “Experimental evidence of inertial waves in a precessing spheroidal cavity,” *Geophys. Res. Lett.* **28**, 3785–3788 (2001).
- <sup>20</sup>J. Noir, P. Cardin, D. Jault, and J.-P. Masson, “Experimental evidence of non-linear resonance effects between retrograde precession and the tilt-over mode within a spheroid,” *Geophys. J. Int.* **154**, 407–416 (2003).
- <sup>21</sup>W. Mouhali, T. Lehner, J. Léorat, and R. Vitry, “Evidence for a cyclonic regime in a precessing cylindrical container,” *Exp. Fluids* **53**, 1693–1700 (2012).
- <sup>22</sup>Y. Lin, J. Noir, and A. Jackson, “Experimental study of fluid flows in a precessing cylindrical annulus,” *Phys. Fluids* **26**, 046604 (2014).
- <sup>23</sup>M. Le Bars, A. Barik, F. Burmann, D. P. Lathrop, J. Noir, N. Schaeffer, and S. A. Triana, “Fluid dynamics experiments for planetary interiors,” *Surveys in Geophysics* **43**, 229 – 261 (2022).
- <sup>24</sup>F. Burmann, L. Kira, and J. Noir, “Precessing non-axisymmetric ellipsoids: bi-stability and fluid instabilities,” *Journal of Fluid Mechanics* **997** (2024), [10.1017/jfm.2024.774](https://doi.org/10.1017/jfm.2024.774).
- <sup>25</sup>J. Léorat, “Large scales features of a flow driven by precession,” *Magneto hydrodynamics* **42**, 143–151 (2006).
- <sup>26</sup>U. R. Christensen and J. Aubert, “Scaling properties of convection-driven dynamos in rotating spherical shells and application to planetary magnetic fields,” *Geophysical Journal International* **166**, 97–114 (2006).
- <sup>27</sup>E. M. King, K. M. Soderlund, U. R. Christensen, J. Wicht, and J. M. Aurnou, “Convective heat transfer in planetary dynamo models,” *Geochemistry, Geophysics, Geosystems* **11** (2010), <https://doi.org/10.1029/2010GC003053>.
- <sup>28</sup>A. Tilgner, “Precession driven dynamos,” *Phys. Fluids* **17**, 034104 (2005).
- <sup>29</sup>C.-C. Wu and P. Roberts, “On a dynamo driven by topographic precession,” *Geophys. Astrophys. Fluid Dyn.* **103**, 467–501 (2009).
- <sup>30</sup>O. Goepfert and A. Tilgner, “Dynamos in precessing cubes,” *New J. Phys.* **18**, 103019 (2016), [10.1088/1367-2630/18/10/103019](https://doi.org/10.1088/1367-2630/18/10/103019).
- <sup>31</sup>C. Nore, J. Léorat, J.-L. Guermond, and F. Luddens, “Nonlinear dynamo action in a

- precessing cylindrical container,” *Phys. Rev. E* **84**, 016317 (2011).
- <sup>32</sup>L. Capanera, J.-L. Guermond, J. Léorat, and C. Nore, “Two spinning ways for precession dynamo,” *Phys. Rev. E* **93**, 043113 (2016).
- <sup>33</sup>A. Giesecke, T. Vogt, T. Gundrum, and F. Stefani, “Nonlinear Large Scale Flow in a Precessing Cylinder and Its Ability To Drive Dynamo Action,” *Phys. Rev. Lett.* **120**, 024502 (2018).
- <sup>34</sup>A. Giesecke, T. Vogt, T. Gundrum, and F. Stefani, “Kinematic dynamo action of a precession-driven flow based on the results of water experiments and hydrodynamic simulations.” *Geophys. Astrophys. Fluid Dyn.* **113**, 235–255 (2019).
- <sup>35</sup>F. Pizzi, A. Giesecke, J. Šimkanin, V. Kumar, T. Gundrum, and F. Stefani, “Numerical and theoretical framework for the dresdyn precession dynamo experiment,” *Magnetohydrodynamics* **58**, 445 – 453 (2022).
- <sup>36</sup>V. Kumar, F. Pizzi, A. Giesecke, J. Šimkanin, T. Gundrum, M. Ratajczak, and F. Stefani, “The effect of nutation angle on the flow inside a precessing cylinder and its dynamo action,” *Phys. Fluids* **35** (2023), 10.1063/5.0134562.
- <sup>37</sup>A. Giesecke, F. Stefani, and G. Gerbeth, “Kinematic simulation of dynamo action by a hybrid boundary-element/finite-volume method,” *Magnetohydrodynamics* , 237 – 252 (2008).
- <sup>38</sup>J.-L. Guermond, R. Laguerre, J. Léorat, and C. Nore, “Nonlinear magnetohydrodynamics in axisymmetric heterogeneous domains using a fourier/finite element technique and an interior penalty method,” *Journal of Computational Physics* **228**, 2739 – 2757 (2009).
- <sup>39</sup>A. Giesecke, C. Nore, F. Stefani, G. Gerbeth, J. Léorat, F. Luddens, and J.-L. Guermond, “Electromagnetic induction in non-uniform domains,” *Geophys. Astrophys. Fluid Dyn.* **104**, 505 – 529 (2010).
- <sup>40</sup>K.-H. Rädler, M. Rheinhardt, E. Apstein, and H. Fuchs, “On the mean-field theory of the karlsruhe dynamo experiment i. kinematic theory,” *Magnetohydrodynamics* **38**, 41 – 71 (2002).
- <sup>41</sup>F. Pizzi, A. Giesecke, and F. Stefani, “Ekman boundary layers in a fluid filled precessing cylinder,” *AIP Advances* **11**, 035023 (2021).
- <sup>42</sup>M. L. Dudley and R. W. James, “Time-dependent kinematic dynamos with stationary flows,” *Proceedings of the Royal Society of London Series A* **425**, 407–429 (1989).
- <sup>43</sup>A. Giesecke, “supplemental material,” will be inserted by publisher (2024).

- <sup>44</sup>M. Wilbert, *Implementation and application of a pseudo-spectral MHD solver combined with an immersed boundary method to support the DRESDYN dynamo experiment*, Ph.D. thesis, Fakultät für Physik und Astronomie der Ruhr-Universität Bochum (2024).
- <sup>45</sup>S. Kreuzahler, D. Schulz, H. Homann, Y. Ponty, and R. Grauer, “Numerical study of impeller-driven von Kármán flows via a volume penalization method,” [New J. Phys. \*\*16\*\*, 103001 \(2014\), 10.1088/1367-2630/16/10/103001](#).
- <sup>46</sup>S. Kreuzahler, Y. Ponty, N. Plihon, H. Homann, and R. Grauer, “Dynamo enhancement and mode selection triggered by high magnetic permeability,” [Phys. Rev. Lett. \*\*119\*\*, 234501 \(2017\)](#).
- <sup>47</sup>A. Giesecke, “supplemental material,” will be inserted by publisher (2024).
- <sup>48</sup>S. Miralles, N. Plihon, and J.-F. Pinton, “Lorentz force effects in the bullard–von kármán dynamo: saturation, energy balance and subcriticality,” [J. Fluids Mech. \*\*775\*\*, 501–523 \(2015\)](#).
- <sup>49</sup>Y. Lin, P. Marti, J. Noir, and A. Jackson, “Precession-driven dynamos in a full sphere and the role of large scale cyclonic vortices,” [Phys. Fluids \*\*28\*\*, 066601 \(2016\)](#).
- <sup>50</sup>K. S. Reddy, B. Favier, and M. Le Bars, “Turbulent kinematic dynamos in ellipsoids driven by mechanical forcing,” [Geophysical Research Letters \*\*45\*\*, 1741 – 1750 \(2018\)](#).
- <sup>51</sup>K. Subramanian, “Hyperdiffusion in nonlinear large- and small-scale turbulent dynamos,” [Phys. Rev. Lett. \*\*90\*\*, 245003 \(2003\)](#).
- <sup>52</sup>R. Avalos-Zuniga, F. Plunian, and A. Gailitis, “Influence of electromagnetic boundary conditions onto the onset of dynamo action in laboratory experiments,” [Phys. Rev. E \*\*68\*\*, 0663071 \(2003\)](#).
- <sup>53</sup>R. Avalos-Zuñiga and F. Plunian, “Influence of inner and outer walls electromagnetic properties on the onset of a stationary dynamo,” [European Physical Journal B \*\*47\*\*, 127–135 \(2005\)](#).
- <sup>54</sup>M. Etchevest, M. Fontana, and P. Dmitruk, “Behavior of hydrodynamic and magnetohydrodynamic turbulence in a rotating sphere with precession and dynamo action,” [Physical Review Fluids \*\*7\*\*, 103801 \(2022\)](#).
- <sup>55</sup>K. Richardson, R. Hollerbach, and M. Proctor, “From large-scale to small-scale dynamos in a spherical shell,” [Phys. Fluids \*\*24\*\*, 107103 \(2012\)](#).
- <sup>56</sup>D. Hughes, F. Cattaneo, and J.-C. Thelen, *Dynamo and Dynamics, a Mathematical Challenge*, NATO Science Series (Kluwer Academic Publishers, Dordrecht / Boston / London,

2001).